Abstract

Keywords:

1. Introduction

The search for alternate energy sources which could be categorised under the "green" label has become important area of research in the modern word. Solar, wind power and wave power are some of the examples of these sources. Recently,a new branch of research has been developing to extract energy from flow induced vibrations(Bernitsas et al. (2008)). It has been hypothesized that this technique may work efficiently in areas where regular turbines cannot.

An elastically mounted slender structure such as cylinders which are susceptible to flow-induced vibrations has the potential for energy extraction. With regards to a slender body two common types of flow induced vibrations are Vortex Induced Vibrations (VIV) and aeroelastic galloping. Significant research has been carried out by Bernitsas and his team on extracting useful energy from VIV. Some of their significant work includes investigating the influence of physical parameters such as mass ratio, Reynolds number, mechanical properties(Raghavan and Bernitsas (2011) ,Lee and Bernitsas (2011)) and location (effect of the bottom boundary) (Raghavan et al. (2009)). However,the possibility of extracting energy using aeroelastic galloping has not been thoroughly investigated. Some theoretical work was carried out by (Barrero-Gil et al. (2010)). Utilizing galloping may be a more viable method to harness energy from flow induced vibrations as it is not bounded by a narrow "lock-in" range of reduced velocities(ratio between the freestream velocity and the product of the natural frequency of the system and the characteristic length). This study further explores the possibility of harnessing energy from flow induced vibrations using aeroelastic galloping.

Energy harvesting systems have high damping ratios because the energy generator (e.g electrical generator) puts a significant amount of damping into the system. Therefore it is crucial to investigate the behaviour of aeroleastic galloping scenarios at high damping ratios in order to optimise the system to obtain a acceptable power output.Hence the focus of this paper is concentrated on investigating the mechanical power output of high-damped galloping systems.

According to Païdoussis et al. (2010),Glauert (1919) has provided a criterion for galloping by considering the auto-rotation of an aerofoil. Den Hartog (1956) has provided a theoretical explanation for galloping for iced electric transmission lines. A non-linear theoretical aeroelastic model to predict the response of galloping was developed by Parkinson and Smith (1964) based on the quasi-steady state (QSS) theory. Experimental lift and

drag data on a fixed square prism at different angles of attack were used as an input for the theoretical model. It essentially used a curve fit of the transverse force to predict the galloping response. The study managed to achieve a good agreement with experimental data. The QSS model equation when solved using analytically using sinusoidal solution mehod cannot predict cases with low mass ratios .Joly et al. (2012) have observed that finite element simulations shows a sudden change in amplitudes below a critical values of the mass ratio. The Parkinson's equation was essentially modified to account for the vortex shedding and managed to produce the effects to the amplitude at low mass ratios. Barrero-Gil et al. (2010) have investigated the possibility of extracting power from vibrations caused by galloping using quasi-steady state theory. In the conclusions of that paper it was pointed out that in order to obtain a high power to area ratio the mass-damping ($m^*\zeta$) parameter should be kept low as well as the frequency of oscillations should be carefully matched have a good agreement with the size of the cross section . Another interesting conclusion was that energy conversion systems which uses galloping could operate over a large range of flow velocities unlike VIV energy harvesting systems where the factor of energy conversion has a strong dependence on the incoming flow velocity. **Nomenclature**

a_1, a_3, a_5, a_7	coefficients of the polynomial to determine C_y
C_y	instantaneous lift
F_y	force due to C_y
ρ	fluid density
m	mass of the body
m_a	added mass
c	damping constant/damping factor
k	spring constant
U_i	induced velocity
θ	induced angle of incidence
U	freestream velocity
$y, \dot{y}, \ddot{y}$	transverse displacement, velocity and acceleration
A	displacement amplitude
$\mathcal{A}$	cross sectional area
F_0	force due to shedding
ω_s	vortex shedding frequency
t	time
P_{mean}	mean power
$f = \frac{1}{2\pi}\sqrt{\frac{k}{m}}$	natural frequency of the system
$\omega_n = 2\pi f$	natural frequency of the system
D	characteristic length of the body
$m^* = \frac{m}{\rho \times \text{Volume of the body}}$	mass ratio
$U^* = \frac{U}{f \times D}$	reduced velocity
$\zeta = \frac{c}{2m\omega_n}$	damping ratio
P_t	power transferred to the body by the fluid
P_d	power dissipated due to mechanical damping
Re	Reynolds number
$\theta = \tan^{-1}\left(\frac{\dot{y}}{U}\right)$	instantaneous angle

2. Background theory

2.1. Mathematical model (Quasi-steady)

One of the widely used mathematical model to predict the system response under galloping is the Quasi-steady state (QSS) model, incorporated by Parkinson and Smith (1964) for a square cross section. The equation of motion of the body under galloping is given by Eq. (1). The forcing term F_y is given by Eq.(2).

$$(m + m_a)\ddot{y} + c\dot{y} + ky = F_y \tag{1}$$

$$F_y = \frac{1}{2}\rho U^2 \mathcal{A} C_y \tag{2}$$

Figure 1: Induced angle of attack on the square prism due to the resultant of free-stream velocity of the fluid and transverse velocity of the body.

In the QSS model C_y is determined by an interpolating polynomial based on the lift and drag data for flow over a stationary body at various angles of attack. The order of the interpolation polynomial has varied from study to study. For example a 7th polynomial order was used in Parkinson and Smith (1964) and 3rd order polynomial was used in Barrero-Gil et al. (2009). Ng et al. (2005) concluded that using a 7th order polynomial is sufficient and a polynomial higher than that of 7th order polynomial neither provides a significantly better result nor does it exhibit an additional amplitudes of oscillation. Thus a 7th order interpolating polynomial was incorporated in this present study.

$$C_y(\theta) = a_1 \left(\frac{\dot{y}}{U} \right) + a_3 \left(\frac{\dot{y}}{U} \right)^3 + a_5 \left(\frac{\dot{y}}{U} \right)^5 + a_7 \left(\frac{\dot{y}}{U} \right)^7 \tag{3}$$

Joly et al. (2012) introduced an addition of a sinusoidal forcing function to the hydro-dynamic forcing. This enables to model to provide accurate predictions even at low mass ratios where galloping excitation is suppressed or not present. In this study, the forcing due to VIV is incorporated using a sinusoidal forcing function $F_0 \sin \omega_s t$ added to the RHS of the equation. ω_s and F_0 represents shedding frequency and the maximum force due to shedding respectively. Thus, the final equation is given by Eq. (4).

$$(m+m_a)\ddot{y}+c+\dot{y}+ky=\frac{1}{2}\rho U^2 \mathcal{A} \left(a_1 \left(\frac{\dot{y}}{U} \right) +a_3 \left(\frac{\dot{y}}{U} \right)^3 +a_5 \left(\frac{\dot{y}}{U} \right)^5 +a_7 \left(\frac{\dot{y}}{U} \right)^7 \right) +F_0 \sin (\omega_s t)$$
$$\tag{4}$$

This equation could be solved by time integration methods. In this study 'Ode 45' routine in MATLAB was used to obtain the solutions.

2.2. Calculation of average power

The dissipated power due to the mechanical damping represents the ideal potential amount of harvested power output. Therefore the mean power output could be given by Eq. (5).

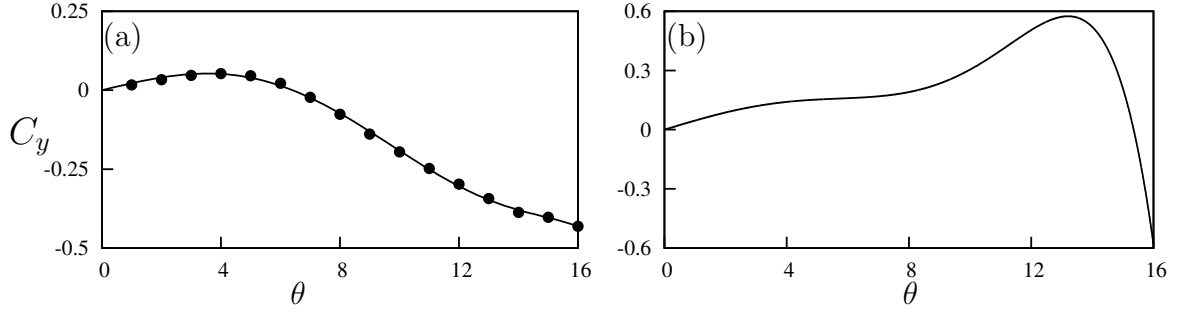$$P_{mean} = \frac{1}{T} \int_0^T (c\dot{y})\dot{y}dt \tag{5}$$

4

Figure 2: Lift coefficient, C_y **JL: C_y is upper case here, lower case on the figure. Make them match what is in the nomenclature **, as a function of incidence angle θ, for a static square cross section. (a) Data from simulations at $Re = 165$ (b) data from Parkinson and Smith (1964) at $Re = 22300$. Points ($\bullet$) are measurements from the simulations. The solid lines in both plots are 7th-order interpolating polynomial used to predict the fluid forcing for the QSS model.

Case	a_1	a_3	a_5	a_7
Re=165	1.3	125.3	1825.73	8765.3
Re=22300	2.69	168	1670	59900

Table 1: Coefficient values used in the 7th order interpolation polynomial for high ($Re = 22300$) and low ($Re = 165$) Reynolds numbers. These data are used as input data to calculate the RHS of Eq.4 throughout this study.

2.3. Parameters used

The stationary data and the fluid-structure interaction (FSI) data were obtained using a higher order spectral element code to simulate the two-dimensional laminar flow. The Reynolds number was kept at 165 as it was pointed out by Sheard et al. (2009) and Tong et al. (2008) that the 3 dimensional transition for a square cylinder occurs at approximately Re=160. F_0 was kept at 0.4937 which was obtained by scaling the value used by Joly et al. (2012) with the amplitude ratios of the lift forces obtained at the different Reynolds numbers.

Shedding frequency ω_s, was set to 0.98 winch was obtained by performing a power spectral analysis of the stationary data at 0^0. Stationary C_y data were obtained at different angles of attack ranging from 0^0 to 16^0. The average power was obtained by using Eq. (5) and the averaging was done over no less than 20 galloping periods. Predictions of power output at Re=22300 were obtained using coefficients for curve fitting C_y (1) from Parkinson and Smith (1964) in order to provide a comparison between high and low Reynolds numbers. m^* was kept at 1163 for Re=22300 (Similar as Parkinson and Smith (1964)) and $m^* = 20$ for Re=165. These parameters were used throughout this study unless otherwise specified.

5

FSI data were obtained for the oscillating (free-vibration) scenario. The Naiver-Stokes equations were solved using an accelerated frame of reference using the previously mentioned code. A three-step time splitting scheme together with high-order Lagrangian polynomials were used to obtain the solution. The details of the method could be found in Thompson et al. (2006, 1996). This code was incorporated in Leontini et al. (2011, 2007) where it was employed in a fluid-structure interaction problems.

The computational domain consists of 690 quadrilateral macro elements where majority of the elements were concentrated near the square section. A freestream condition was given to the inlet, top and bottom boundaries and the normal velocity gradient was set to zero at the outlet. A convergence study was performed by changing the order of the polynomial (p-refinement) at $U^* = 40$ and Re 165. A 9th order polynomial together with a time step of $\frac{\Delta t U}{D} = 0.001$ was sufficient to ensure an accuracy of 2% with regards to amplitude of oscillation.

3. Results

3.1. Stationary data

The stationary C_y data obtained using flow simulations (Fig.3(a))have a good agreement with data presented in Joly et al. (2012). In comparison with the 7th order polynomial curve at Re=22300 (Fig.3(b)) several differences could be observed. The peak value of C_y is significantly low at Re=165 ($C_y = 0.05$ at 4^0) in comparison with Re=22300 ($C_y = 0.57$ at 13^0) . The inflection point present at Re=22300 could not be observed at Re=165. This agrees with the findings of Luo et al. (2003). It was concluded by Luo et al. (2003) that hysteresis occur due to the inflection point found in the C_y curve. Therefore hysteresis is not expected at Re=165. The range of the incident flow angles where C_y remain positive is narrow at Re=165 ($0^0 < \theta \leq 6^0$) compared to Re=22300 ($0^0 < \theta \leq 15^0$). This feature is what sustains galloping and power is transferred from the fluid to the supporting structure within this range of incident angle because fluid forces are acting in the direction of travel of the oscillating cylinder. Incident angles beyond this range actually suppresses the galloping and power goes in the opposite direction. Therefore due to the overall smaller C_y and narrow range of angles where C_y is positive for Re=165 compared to Re=22300 leads one to expect a significant reduction in power atRe=165 compared to Re=2230.

3.2. Displacement,velocity and power output as a function of reduced velocity

The quasi-steady analysis data reveals that the displacement amplitude tend to grow with increasing U^* Fig.3 (a) and (b). The onset of galloping is delayed with increasing ζ for both high and low Reynolds numbers. This echo the findings of previous studies by Parkinson and Smith (1964) and Barrero-Gil et al. (2010). Hysteresis could be observed for the case with a higher Reynolds number.

Power vs U^*

The mean power grows, peaks and then reduces as U^* is increased (Fig.3 (e) and (f)) for each value of ζ. The value of U^*at which the peak power occurs increases with ζ.
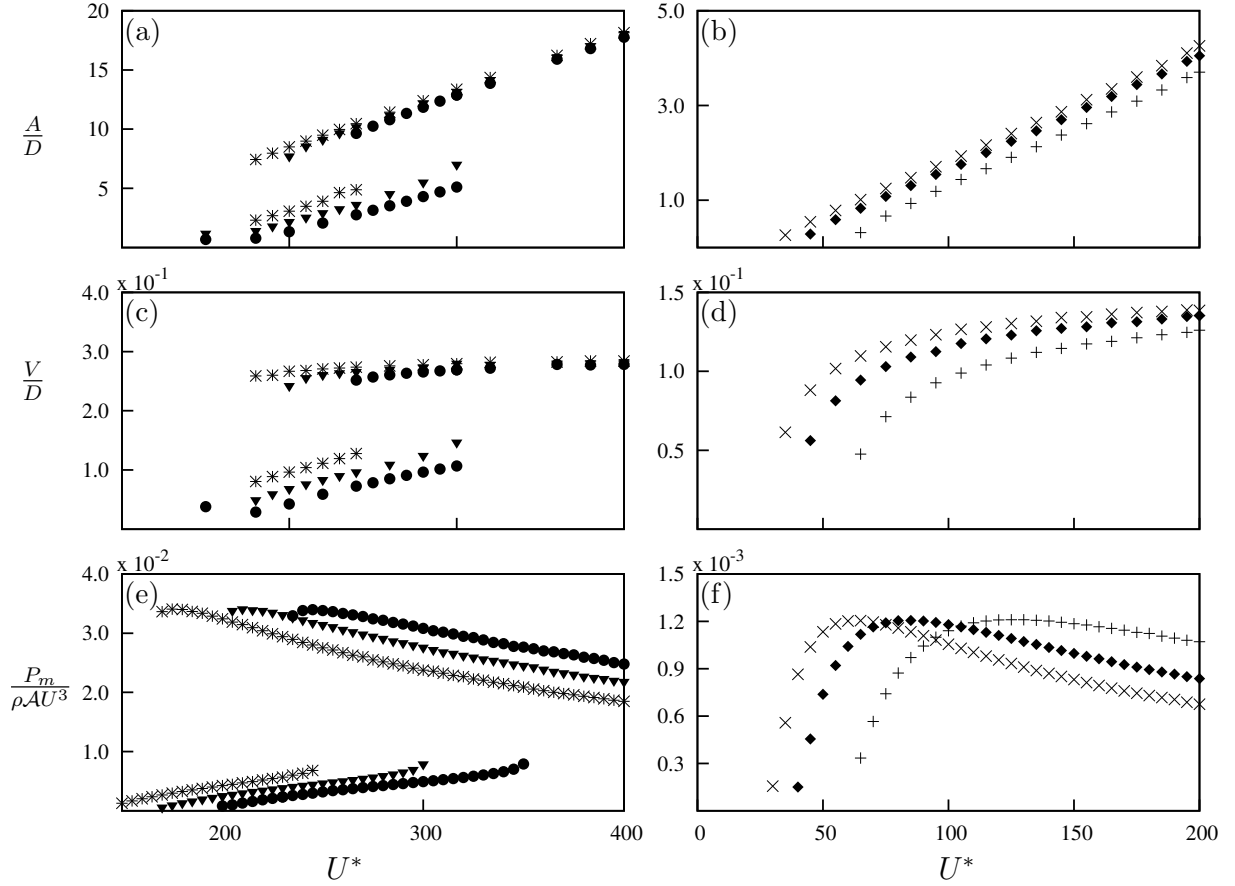
Figure 3: Velocity amplitude, displacement amplitude and mean power as functions of U^*. Data presented in (a), (c) and (e) were calculated using input data at $Re = 22300$ obtained by Parkinson and Smith (1964) at three different damping ratios: $\zeta = 0.0125$ (✳), $\zeta = 0.015$ (▼) and $\zeta = 0.0175$ (●). Data presented in (b),(d) and (f) were obtained using input data at $Re = 165$ at three different damping ratios: $\zeta = 0.075$ (×), $\zeta = 0.1$ (◆) and $\zeta = 0.15$ (+). The multiple branches for the higher Re are due to the hysteresis between two solutions.

However, the magnitude of the peaks remain constant for all the values of ζ. Barrero-Gil et al. (2010) also showed a similar trend. The higher Reynolds number case clearly showed the hysteresis range starting from marginally before the peak value and extend for about the U^*values . It could be observed that unlike VIV the system has no preferred frequency. Although the onset of galloping and the point where peak power occur at different U^* when the damping ratio is changed, the peak power remains constant regardless of U^*.

3.3. Galloping response and natural frequency

Now the oscillator equation Eq.(4) is considered from a power perspective. The shedding forces can be neglected because the net effect is negligible as system oscillates at natural frequency which is far from shedding frequency, for the cases that exhibit galloping. It is obvious that the forcing term on LHS of the equation is only dependent on transverse velocity($\dot{y}$) which is essentially the input power of the system. On the RHS, the mechanical damping or system damping is the only term that takes out power at any instant. This could be expressed as the product of damping force and the velocity (P_d). The inertia and the stiffness terms governs the frequency of the system but the forces associated by those terms are conservative forces (i.e there is zero net energy in or out of the system when averaged over a period). Therefore the system is governed by the transverse velocity rather than the natural frequency.

Using U^* and ζ assumes that the system has a preferred frequency because they scale with the natural frequency of the system. The effect of fixing ζ and increasing U^* actually decreases the damping constant for a fixed free-stream velocity. ($U^* = \frac{U}{f \times D}$, $\zeta = \frac{c}{2m\omega_n}$). Both these effects leads to the multiple lines that are horizontally transpose when ζ is increased (Fig.3 (e) and (f)). Therefore the effect of ζ essentially scales up the damping coefficient for a fixed U^*.

The data presented in 3 for various damping ratios ,ζ, can be collapsed into a single line for a for a particular force characteristic curve (i.e C_y vs θ curve) curve could be obtained for the velocity amplitude and power were plotted as a function of non dimensionalised damping constant c (Fig 4 (a),(b),(c) and (d)). This further emphasizes that the galloping system is not frequency dependent. It is possible to obtain a different similar power output at different values of $U^*$when the damping constant ⋯, is kept fixed. An example of this case, as shown in Fig.5, clearly show that this is a result of similar velocity amplitudes between cases if one were to disragard the high frequencies due to shedding. As mentioned earlier, it is the transverse velocity that determines the energy provided by the fluid forcing and the mechanical damping.

Power could be expressed as the product of force and velocity. Therefore the transferred power form fluid-to-body could be expressed as $P_t = F_y\dot{y}$. Similarly the dissipated power due to the mechanical damping could be expressed as $P_d = (c\dot{y})\dot{y}$. The time average of these two quantities should be equal due to energy conservation, provided that the mechanical friction is neglected . Analysing the time histories of P_t and P_d at key regions (Fig.6) on the mean power vs U^* provides a detailed explanation for the variation of the output powe when the reduced velocity is increased. The key regions consists of region 1 where
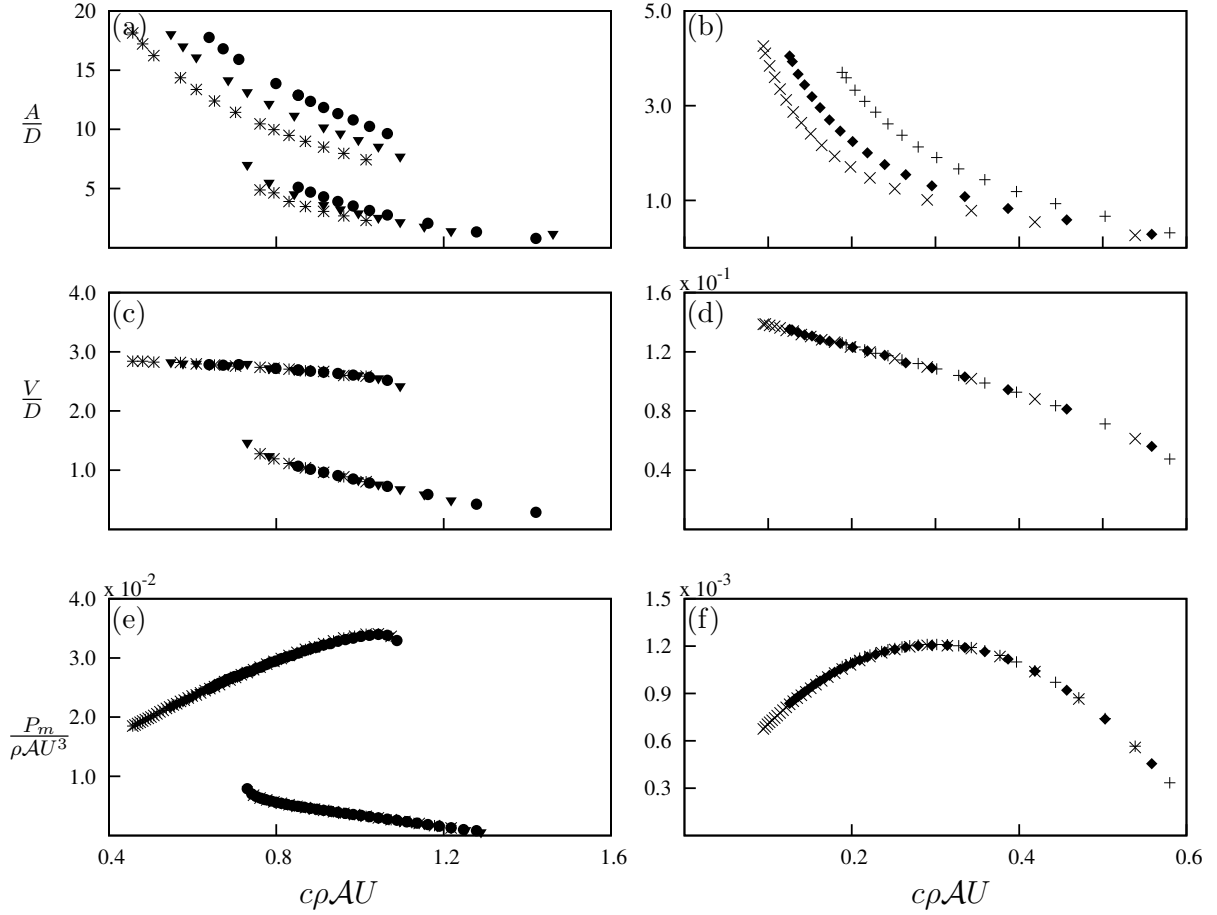
Figure 4: Displacement amplitude, velocity amplitude and mean power as functions of the damping factor. Data presented in (a),(c) and (e) were calculated using input data at $Re = 22300$ obtained by Parkinson and Smith (1964) at three different damping ratios: $\zeta = 0.0125$ (∗), $\zeta = 0.015$ (▼) and $\zeta = 0.0175$ (●). Data presented in (b), (d) and (f) were obtained using input data at $Re = 165$ at three different damping ratios: $\zeta = 0.075$ (×), $\zeta = 0.1$ (◆) and $\zeta = 0.15$ (+). The collapsed data implies that there is no frequency selection and the tuning parameter of the mechanical side of the system is the damping constant to obtain an optimum power output.
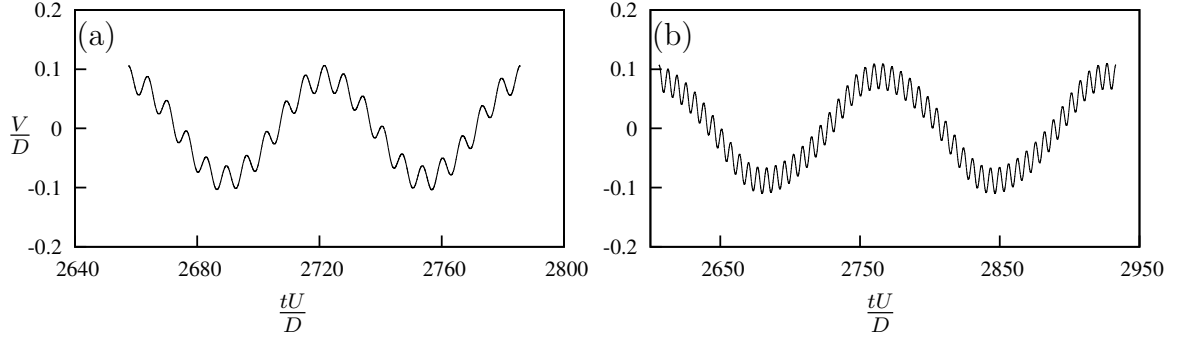
Figure 5: Time histories of velocity at two different ζ and U^* which produce the same mean power (1.2×10^{-3}). Data presented in (a) are at $U^* = 60$, $\zeta = 0.075$ and (b) are at $U^* = 165$, $\zeta = 0.175$. Both data sets were obtained using Quasi-steady state assumption using input C_y parameters at $Re = 165$. Shedding is evident in both signals as a high frequency fluctuation but the amplitude of the slower fluctuations remains constant in both cases.

the P_m increases with U^*, region 2 where P_m becomes maximum and region 3 where P_m decreases with U^*. It has been established earlier that the damping factor is a function of U^*. Therefore it could be derived that U^* is inversely proportional to damping coefficient. Hence the damping coefficient reduces when you move from region 1 to 3.Fig 2 (a) shows that C_y and therefore instantaneous force rises until 4^0 where it peaks and then falls and at around 6^0 becomes negative. Maximum amount of power could be transferred within the peak region. At the region where the instantaneous force becomes negative it will be opposing the velocity $\dot{y}$.Data at $\zeta = 0.1$, $m^* = 40$ and $Re=165$ (Fig.7) are analysed as and example.

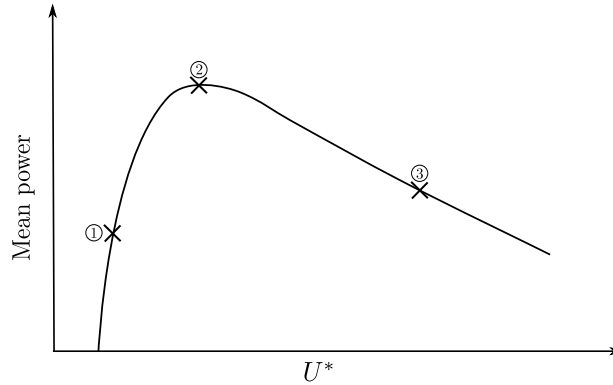
Figure 6: Three key regions taken into account to analyse the time histories of power in a typical mean power vs. U^* curve at $Re = 165$. In region 1, high damping suppresses oscillation, hence the power output is low. In region 2, the damping is close to the optimum for power transfer. In region 3, the low damping means little energy is extracted from the fluid.

At region 1 where $U^* = 90$ the damping constant is high and a clear sinusoidal signal could be observed for both P_d and P_t in Fig. 7 (a). Fig.7 (d) and (g) shows that θ is in
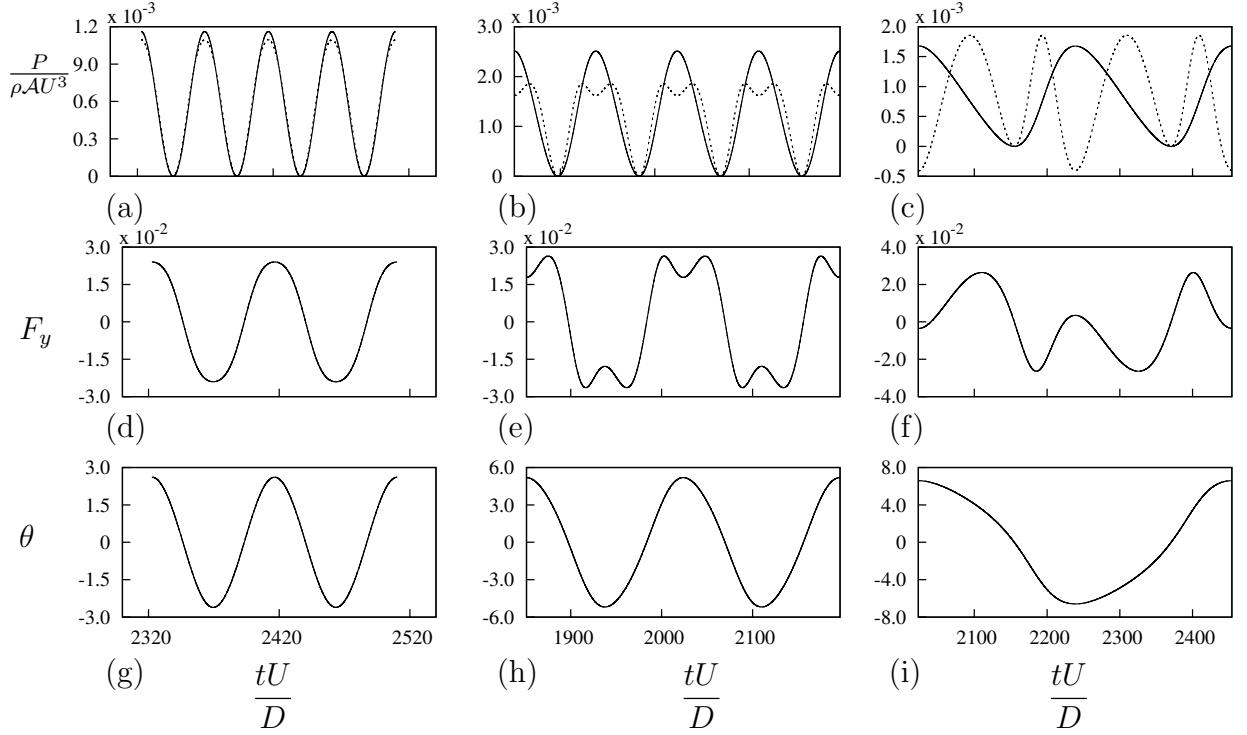
Figure 7: Time histories of P_t, P_d, F_y and θ at $U^* = 90$, 165 and 400. Data was obtained at $\zeta = 0.1$, $m^* = 40$ and $Re = 165$. The time histories of P_t (—) and P_d (- - -) are presented for: (a) $U^* = 90$; (b) $U^* = 165$; (c) $U^* = 400$. Time histories of the instantaneous force F_y for: (d) $U^* = 90$; (e $U^* = 165$; (f) $U^* = 400$. Time histories of the instantaneous angle θ for: (g) $U^* = 90$; (h) $U^* = 165$; (i) $U^* = 400$.

line or in phase with F_y. The velocity amplitude in this case is small and the equivalent incident angle within the range where the hydrodynamic foce increases with the incident angle (i.e. $0 < \theta \leq\leq 4^0$ in 2) Hence both P_d and P_t becomes sinusoidal. In this case, power output is limited by the low fluid forces present at lwo incident angles.

At region 3 ($U^* = 400$) 'c' is low in comparison with region 1 and 2 which leads to a low mean power output. Fig.7 (c) shows that P_t becomes negative over some portion of the cycle. This is because θ passes the point where both θ and C_y (therefore F_y) are positive. The high velocity amplitude leads to the equivalent incident angle θ, in this case to exceed the range where C_y is positive (i.e. $0 < \theta < 6^0$)

At region 2 ($U^* = 165$) the mean power output is at its maximum. P_t is not a pure sinusoidal signal. However, the signal remains periodic. From the time history graph of P_t, two 'peaks' are present in a single half cycle (Fig 7 (b)). In this case, the velocity amplitude actually exceeds the equivalent incident angle where the hydrodynamic forces peaks (i.e. $\theta = 4^0$ in 3 (a)). The dips in P_d between the two peaks approximately correspond to the time where the transverse velocity is higher than 0.07 and F_y is decreasing with increasing transverse velocity.
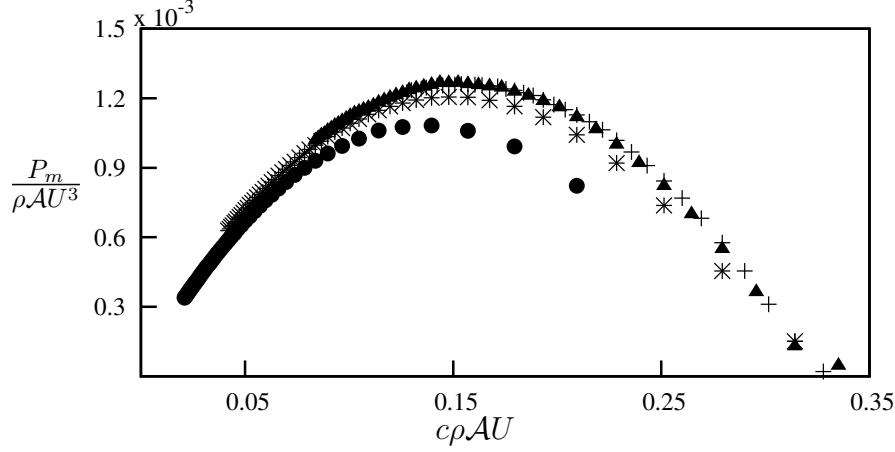
11

Figure 8: Mean power as a function of damping factor. Data are presented at $m^* = 10$ (●), $m^* = 20$ (✳), $m^* = 40$ (▲), $m^* = 60$ (+) at Re 165 and $\zeta = 0.1$. A reduction of maximum mean power can be observed when $m^* < 40$. For $m^* > 40$, the maximum power is essentially independent of m^*.
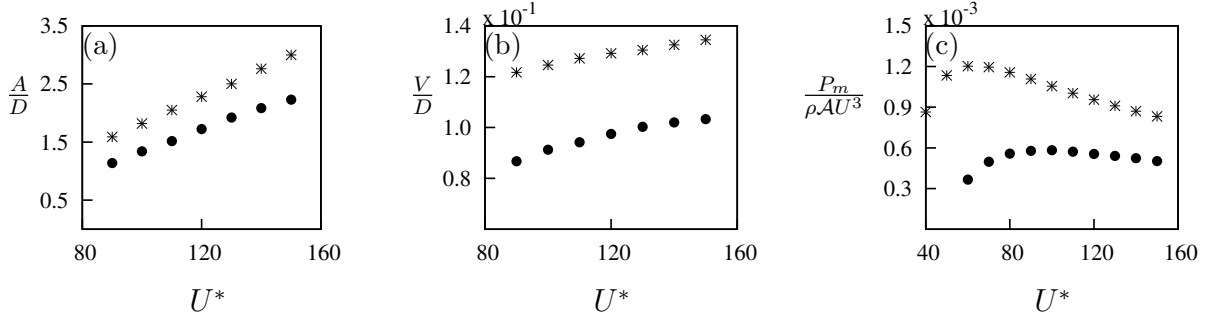

Figure 9: Comparison of data generated using the quasi-static theory (✳) and full DNS simulations (●). (a) Displacement amplitude, (b) velocity amplitude and (c) mean power as functions of U^*. Data were obtained at $Re = 165$ and $\zeta = 0.075$. An average difference of 34% is observed for both displacement and velocity amplitude. However, the essential physics i.e the rise and fall of mean power, is captured by DNS simulations.

3.4. Effect of m^*

The maximum mean power at different m^* (Fig.8) was constant beyond $m^* = 30$. However, at $m^* \leq 30$ an effect of m^* it could be observed. The peak value of the mean power curve reduces with m^*. This may be due to the fact that as the inertia of the system is reduced and galloping becomes weak. Therefore shedding become dominant. This was also reported by Joly et al. (2012) where galloping amplitude was reduced at low m^*.

3.5. Comparison with FSI simulations

Similar trends were captured for both displacement and velocity amplitudes between QSS and FSI simulations (Fig. 9(a) and 9(b)). Quantitatively a large discrepancy (average of 30%) could be observed between QSS and FSI data. Therefore the power also becomes significantly low in FSI data (Fig.9(c)). However, the FSI data (Fig.9 (c)) were able to produce the main the rise and the fall of mean power when U^* was increased. The

reasoning behind this fact is that galloping is weak at Re 165 and therefore fluid damping has a significant effect. It was reported by Barrero-Gil et al. (2009) that galloping only starts to occur ar Re $\geq$ 159. As power is function of $(\dot{y})^2$ the error between QSS and FSI power becomes significantly large.

Put conclusion here

Barrero-Gil, A., Alonso, G., Sanz-Andres, A., Jul. 2010. Energy harvesting from transverse galloping. Journal of Sound and Vibration 329 (14), 2873–2883.

Barrero-Gil, a., Sanz-Andrés, A., Roura, M., Oct. 2009. Transverse galloping at low Reynolds numbers. Journal of Fluids and Structures 25 (7), 1236–1242.

Bernitsas, M. M., Raghavan, K., Ben-Simon, Y., Garcia, E. M. H., 2008. VIVACE (Vortex Induced Vibration Aquatic Clean Energy): A new concept in generation of clean and renewable energy from fluid flow. Journal of Offshore Mechanics and Arctic Engineering 130 (4), 041101–15.

Den Hartog, J. P., 1956. Mechanical Vibrations. Dover Books on Engineering. Dover Publications.

Glauert, H., 1919. The rotation of an aerofoil about a fixed axis. Tech. rep., Advisory Committee on Aeronautics R and M 595. HMSO, London.

Joly, A., Etienne, S., Pelletier, D., Jan. 2012. Galloping of square cylinders in cross-flow at low Reynolds numbers. Journal of Fluids and Structures 28, 232–243.

Lee, J., Bernitsas, M., Nov. 2011. High-damping, high-Reynolds VIV tests for energy harnessing using the VIVACE converter. Ocean Engineering 38 (16), 1697–1712.

Leontini, J. S., Lo Jacono, D., Thompson, M. C., Nov. 2011. A numerical study of an inline oscillating cylinder in a free stream. Journal of Fluid Mechanics 688, 551–568.

Leontini, J. S., Th, M. C., Hourigan, K., Apr. 2007. Three-dimensional transition in the wake of a transversely oscillating cylinder. Journal of Fluid Mechanics 577, 79.

Luo, S., Chew, Y., Ng, Y., Aug. 2003. Hysteresis phenomenon in the galloping oscillation of a square cylinder. Journal of Fluids and Structures 18 (1), 103–118.

Ng, Y., Luo, S., Chew, Y., Jan. 2005. On using high-order polynomial curve fits in the quasi-steady theory for square-cylinder galloping. Journal of Fluids and Structures 20 (1), 141–146.
URL http://linkinghub.elsevier.com/retrieve/pii/S0889974604001215

Païdoussis, M., Price, S., de Langre, E., 2010. Fluid-Structure Interactions : Cross-Flow-Induced Instabilities. Cambridge University Press.

Parkinson, G. V., Smith, J. D., 1964. The square prism as an aeroelastic non-linear oscillator. The Quarterly Journal of Mechanics and Applied Mathematics 17 (2), 225–239.

Raghavan, K., Bernitsas, M., Apr. 2011. Experimental investigation of Reynolds number effect on vortex induced vibration of rigid circular cylinder on elastic supports. Ocean Engineering 38 (5-6), 719–731.

Raghavan, K., Bernitsas, M. M., Maroulis, D. E., 2009. Effect of Bottom Boundary on VIV for Energy Harnessing at $8 \times 10^3 < Re < 1.5 \times 10^5$. Journal of Offshore Mechanics and Arctic Engineering 131 (3), 031102.

Sheard, G. J., Fitxgerald, M. J., Ryan, K., Jun. 2009. Cylinders with square cross-section: wake instabilities with incidence angle variation. Journal of Fluid Mechanics 630, 43.

Thompson, M., Hourigan, K., Sheridan, J., Feb. 1996. Three-dimensional instabilities in the wake of a circular cylinder. Experimental Thermal and Fluid Science 12 (2), 190–196. URL http://linkinghub.elsevier.com/retrieve/pii/0894177795000984

Thompson, M. C., Hourigan, K., Cheung, A., Leweke, T., Nov. 2006. Hydrodynamics of a particle impact on a wall. Applied Mathematical Modelling 30 (11), 1356–1369. URL http://linkinghub.elsevier.com/retrieve/pii/S0307904X06000321

Tong, X., Luo, S., Khoo, B., Oct. 2008. Transition phenomena in the wake of an inclined square cylinder. Journal of Fluids and Structures 24 (7), 994–1005. URL http://linkinghub.elsevier.com/retrieve/pii/S088997460800025X